



ELSEVIER

Contents lists available at ScienceDirect

Journal of Hydrology

journal homepage: www.elsevier.com/locate/jhydrol

Research papers

Heat tracer test in a riparian zone: Laboratory experiments and numerical modelling



Jie Ren^{a,b,*}, Xiuping Wang^a, Zhenzhong Shen^b, Jian Zhao^b, Jie Yang^a, Ming Ye^c, Yinjun Zhou^d, Zhenhua Wang^e

^a State Key Laboratory of Eco-hydraulics in Northwest Arid Region of China, Xi'an University of Technology, Xi'an 710048, Shaanxi, China

^b State Key Laboratory of Hydrology-Water Resources and Hydraulic Engineering, Hohai University, Nanjing 210098, Jiangsu, China

^c Department of Earth, Ocean, and Atmospheric Science, Florida State University, Tallahassee 32306, FL, USA

^d Changjiang River Scientific Research Institute, Wuhan 430010, Hu Bei, China

^e College of Water & Architectural Engineering, Shihezi University, Shihezi City 832000, Xinjiang, China

ARTICLE INFO

This manuscript was handled by Corrado Corradini, Editor-in-Chief, with the assistance of Subashisa Dutta, Associate Editor

Keywords:

Water temperature
Laboratory experiment
Numerical simulation
Riparian zone

ABSTRACT

The use of water temperature as a tracer has been widely utilized for characterizing the dynamics of water flow and heat transport in riparian zones. By using experimental approaches, we investigated the effects of water temperature, hydraulic head, and heat radiation on water flow and thermal dynamics in riparian zones through sand tank experiments, which simulate the dynamics of water flow and heat transport in riparian zones. Water of low temperature was pumped into the sand tank, and changes of temperature at different locations of the sand tank were measured. Temperature data was examined for three different water temperatures (4.0 °C, 6.0 °C, and 9.5 °C), two different hydraulic heads (25 cm and 45 cm), and two different radiation temperatures (no radiation and 22 °C). The thermal dynamic variation pattern in different types of water temperatures, hydraulic heads, and radiation combinations, was also analyzed using a HYDRUS-2D model. The temperature sensors, located near the inlet infiltration boundary, required a shorter time to reach the steady state, because the temperature declined more rapidly near the inlet. The effect of lateral inflow on the temperature gradient was obvious. The temperature gradient in the horizontal direction gradually decreased, and the vertical temperature gradient gradually increased. In the initial stage of infiltration, the temperature gradient in the horizontal direction was larger than the temperature gradient in the vertical direction, however, as time goes on, the temperature gradient in the vertical direction was larger than the temperature gradient in the horizontal direction. In addition, the horizontal temperature gradient of the top sand layer was less affected by the water temperature. The closer the temperature observation point of the same horizontal section was to the infiltration boundary, the higher the rate of temperature difference changes. Comparison of the predicted and observed thermal dynamics variation of the 2-D sand tank shows good agreement, indicating that the major mechanism for water flow and thermal dynamics variation was hydraulic head. The sensitivity analysis results illustrate that the model was most sensitive to hydraulic head (H), followed by Van Genuchten parameter (α), permeability coefficient (K_s), water temperature (T), Van Genuchten parameter (n), residual moisture content (θ_r), and saturated moisture content (θ_s). The variation of each parameter was linear with the change of temperature field. Parameters which were positively related to the temperature field were T , α , θ_r and θ_s , which means the parameter value becomes larger as the temperature becomes larger, and vice versa. The parameters which were negatively related to the temperature field were H , K_s and n .

1. Introduction

Water temperature is one of the important factors that influences hydrologic and aquatic ecological environments. Large reservoirs are stratified with depth due to their capacity and slow flow rate. Water temperatures decrease with depth in large reservoirs and temperatures

at the deepest layer remain constant all year. Release of low-temperature water from reservoirs can impact downstream aquatic environments. For example, the water temperature was low in discharges from reservoirs in spring and summer (Preece and Jones, 2002; Prats et al., 2010), and it was high in winter (Maheu et al., 2016). The low-temperature water from large reservoirs had an extremely important

* Corresponding author at: State Key Laboratory of Eco-hydraulics in Northwest Arid Region of China, Xi'an University of Technology, Xi'an 710048, Shaanxi, China.
E-mail address: renjie@xaut.edu.cn (J. Ren).

impact on aquatic organisms and even aquatic ecosystems downstream of the dam.

Using groundwater temperature as a natural tracer, as opposed to using a chemical tracer, reduces negative impacts on the aquatic environment (Anderson, 2005; Constantz, 2008). In recent studies, water temperature as a natural tracer was used extensively to estimate heat exchange processes (Xie et al., 2015; Klepikova et al., 2016), groundwater discharges to surface waters (Duque et al., 2016), SW/GW interactions (Hyun et al., 2011; Naranjo and Turcotte, 2015; Munz et al., 2016; Schneidewind et al., 2016), and aquifer characteristics (Wildemeersch et al., 2014; Doro et al., 2015; Sakata, 2015; Colombani et al., 2015; Klepikova et al., 2016). Duque et al. (2010) studied the relations between rivers and the associated aquifers using groundwater temperature measurements, and general data on river discharge, and environmental and river temperatures. Sellwood et al. (2015) used in-well heat tracer tests to estimate borehole fluid flow rates and to evaluate the range of flow rates. Although the on-site thermal tracing test has yielded positive results, a more quantitative mechanism analysis is needed for the study of river ecology and solute exchange processes.

In recent years, with the application of automated observation technology, as well as the progress of data processing technology, the effects of water temperature changes over time on the physical properties of river beds can be more accurately examined. For example, temperature time series methods were extensively used to calculate vertical water fluxes (Keery et al., 2007; Gordon et al., 2012), Darcy velocity (McCallum et al., 2012), and groundwater-surface water exchange (Irvine et al., 2015). Tonina et al. (2014) based on temperature time series of surface and streambed pore waters, monitored local changes in streambed surface elevations at a daily time scale. He found that time series analysis of paired in-stream and pore water temperatures can predict variations in streambed surface elevations at the daily time scale with a 20% accuracy. More recently, Wilson et al. (2016) presented a method that inverts thermal time series data to estimate the timing and depth of transient hydrodynamic exchange. They found that it was possible to identify the depth of flushing using shallow datasets, in which flushing extended below the deepest sensor. This finding was used to estimate the influence of streambed or riverbed sediments on groundwater surface water exchange fluxes (Irvine et al., 2015).

Several research efforts were designed to characterize groundwater discharge to surface waters and ground velocities by performing distributed temperature sensing (DTS). Among them, Mamer and Lowry (2013) represented the initial lab testing of a new combined method to assess the viability of using pairs of DTS time series profiles to quantify and locate zones of discrete groundwater discharge throughout an entire stream reach. Bakker et al. (2015) presented a new methodology for using a heat tracer test to determine groundwater velocities. It inserts fiber optic cables vertically into unconsolidated sedimentary aquifers without the need for boreholes, and to measure temperature along these cables using DTS. Hare et al. (2015) compared thermal infrared to fiber-optic distributed temperature sensing for locating discrete groundwater discharges to surface water.

The above studies show that many scholars have used water temperature as a tracer to study the river-related problems, but the evaluation of water temperature as a tracer to study water flow and thermal variation mechanisms in riparian zones is rarely reported. Somewhat later, Sawyer et al. (2009) monitored water-table elevation, temperature, and specific conductivity along a transect perpendicular to the Colorado River (Austin, Texas, USA), 15 km downstream of the Longhorn dam to evaluate the penetration distance and rates of dam-induced lateral hyporheic exchange paths. They found that wooded riparian zones can reduce stream temperatures, particularly in terms of maximum temperatures. Bowler et al. (2012) conducted a systematic review of the available evidence for the effects of wooded riparian zones on stream temperature to assess the effectiveness of this intervention. They used hydraulic and temperature data to calibrate the

reliable conservative transport model as calibration constraints. Due to the interface between surface water and groundwater in riparian zones and the particularity of the hyporheic location and structure, it is difficult to measure water flow and heat transport in riverbed hyporheic exchange processes. These exchange areas are an important manifestation of the complex edge effect of the riparian zone, which have important protection functions for rivers and groundwater. And it is becoming a hot topic for future research.

Riparian zones played the key role in the function of aquatic ecosystems which could affect the chemical, physical and biological processes. When low-temperature water from a reservoir is released, it infiltrates into the riparian zones, and mixes with natural groundwater allowing for heat exchange. Then, the low temperature water released from the reservoir forms the soil non-isothermal environment under the two-way radiation conditions which consists of the low temperature water layer in lower part and the upper natural temperature surface, and could cause the redistribution of temperature and moisture field inevitably. There were significant changes on riverbed sediment and riparian saturation-unsaturated zone heat state, and these differences could be characterized by groundwater activities. Soil moisture and temperature were the most important influencing factors of geochemical and ecological processes in the unsaturated zone (Halloran et al., 2016). The distribution and variation of soil temperature affects the physical and chemical properties of the soil and the biochemical cycle (Paul et al., 2004; Maurer and Bowling, 2014). Studies have shown that soil temperature changes directly affected the soil respiration rate (Contosta et al., 2016; Wang et al., 2016). Soil respiration was one of the main fluxes of the global carbon cycle and was an important determinant of ecosystem carbon balance (Riveros-Iregui et al., 2007), its strength was second only to primary productivity (Laganier et al., 2012), and it was mainly composed of microbial decomposition of soil organic matter and root respiration (Curtin et al., 2012). Low-temperature water also had adverse effects on downstream cropland irrigation. Yang et al. (2012) concluded that the maximum impact scope of low-temperature water was 55 km and water temperature reached the minimum growth temperature of rice during April and June. The use of engineering or non-engineering measures to manage the reservoir discharge temperature regulation and to reduce the adverse effects of low-temperature water on the environment and ecology has become a major problem in the field.

Recent experimental studies have been concerned with the effect of hydraulic conductivity of silty clay under infiltration of low-temperature water (Ren et al., 2014), the purpose of this study was to develop a process, using the 2-D riparian zone test and to use this new test to evaluate water flow and thermal dynamics in riparian zones using the injection of a heat tracer test. In Section 2, we present a methodology for of laboratory experiments and the numerical modeling utilized in this study. In Section 3, we describe laboratory experimental procedures used to evaluate water flow and thermal dynamics in a sand tank. We also reconstructed a numerical model, using three sets of experiments to calibrate and verify. In addition, we used the sensitivity analysis method to analyze the parameters of the model.

2. Methodology

2.1. Laboratory experiments

Experiments were conducted in a sand tank with a precise heating/cooling control system (see Fig. 1). The total sand tank length is 80 cm. The working sediment-filled section is 60 cm in length, 20 cm wide, and 80 m in height. Water flow in the tank was horizontal (Fig. 1b). The inlet and outlet were furnished with perforated plates and gauze to ensure uniform flow across the entire cross-section without losing any sediment. The perforated plates device at the upstream end minimizes pulsing action and facilitates a smooth flow of water into the study section. The upstream reservoir has two overflow holes, 30 cm and

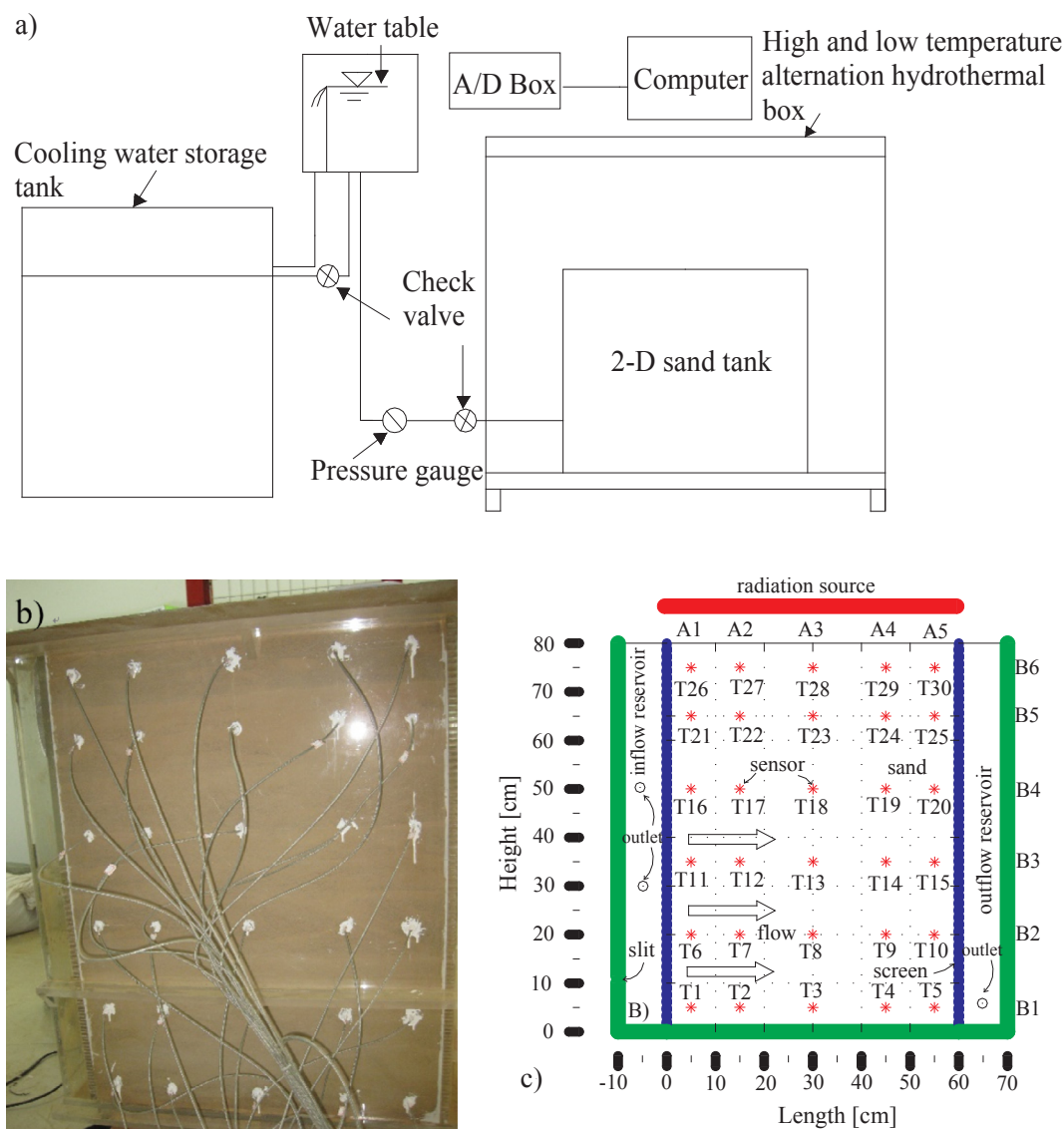


Fig. 1. View of the experimental tank set-up (modified from Ren et al., 2014): (a) Schematic presentation of temperature heating/cooling system, (b) Photograph of 30 temperature sensors are inserted in the sand tank and (c) Scheme of temperature sensors layout of 2-D sand tank.

Table 1
Summary of hydraulic conditions during each low temperature water injection.

	Water temperature (°C)	Hydraulic head (cm)	Radiation (°C)	Duration (min)
Exp1	4.0	25	22	500
Exp2	9.5	25	NA	500
Exp3	6.0	45	22	500

50 cm of the height, respectively. The downstream reservoir has one overflow hole, 5 cm of the height. Prior to each infiltration test, the hydraulic head was kept steady at an initial level of 30 cm or 50 cm from the upstream reservoir of sand tank. The hydraulic head was controlled by the outlet. The sand tank was equipped with a heating and cooling system and the walls and floor insulated to minimize temperature losses. Sand tank infiltration water temperature was controlled by a heating/cooling control system. For each test, a constant infiltration water temperature was applied. Tests were run for three different water temperatures (4.0 °C, 6.0 °C, and 9.5 °C), two different hydraulic heads (25 cm and 45 cm), and two different radiation temperatures (no radiation and 22 °C). The summary of the experiment

conditions is given in Table 1.

In all experiments, the sample used was sand (with the 50th percentile grain diameter $D_{50} = 0.68$ mm and the uniformity coefficient $C_u = 0.5$). Air-dried sand used in the sand tank had an average bulk density of 1.56 g/cm³ and was contained in the high and low temperature alternation hydrothermal box (see Fig. 1). The initial average water content, measured on sand samples taken during packing, was 0.02 cm³/cm³. The initial temperature of the sample was controlled at 20 °C for over 24 h so that the sample had a uniform temperature. During each infiltration test, the data was collected every 1 min from the 30 temperature sensors throughout all three tests. These sensors were connected to an automatic analog signals collector. Signals from temperature sensors were converted into digital signals through an A/D converter. The data were collected by computer continuously. The position of the 30 temperature sensors is shown in Table 2. The temperature data recorded at a frequency of 1 min show how temperature varied temporally and spatially at six locations along the surface. At each location, measurements were taken at six different heights as follows: near the surface (5 cm below the surface: T26, T27, T28, T29, T30); 15 cm below the surface: (T21, T22, T23, T24, T25), mid sand profile (30 cm below the surface: T16, T17, T18, T19, T20); (50 cm

Table 2

Location of temperature sensors. Length indicates the horizontal distance from the left screen boundary and Height indicates the vertical distance from the bottom (Fig. 1c).

Temperature sensor	T1	T2	T3	T4	T5	T6	T7	T8	T9	T10	T11	T12	T13	T14	T15
Length (cm)	5	15	30	45	55	5	15	30	45	55	5	15	30	45	55
Height (cm)	5	5	5	5	5	20	20	20	20	20	30	30	30	30	30
	T16	T17	T18	T19	T20	T21	T22	T23	T24	T25	T26	T27	T28	T29	T30
Length (cm)	5	15	30	45	55	5	15	30	45	55	5	15	30	45	55
Height (cm)	50	50	50	50	50	65	65	65	65	65	75	75	75	75	75

Table 3

Soil thermal parameters used in HYDRUS-2D model.

Solid	Org	D _L cm ² s ⁻¹	D _T	b ₁	b ₂	b ₃	C _n J·g ⁻¹ ·C ⁻¹	C _o	C _w
0.57	0	5	1	4924810	-51969500	106034000	69120000	90360000	150480000

Note: Solid is the ratio of soil solids to total volume, org is the ratio of organic matter to total volume, D_L is longitudinal thermal diffusivity of soil, D_T is horizontal thermal diffusivity of soil, b₁, b₂, b₃ are coefficient of thermal conductivity function, C_n is soil solids heat capacity, C_o is soil organic matter heat capacity and C_w is soil liquid heat capacity.

below the surface: T11, T12, T13, T14, T15) and near the bottom (60 cm below the surface: T6, T7, T8, T9, T10); (75 cm below the surface: T1, T2, T3, T4, T5) as shown in Fig. 1c.

2.2. Numerical modeling

2.2.1. Model description

The numerical model package HYDRUS-2D (Šimunek et al., 2006) was applied in this study to simulate the heat transport processes in the unsaturated sand in the sand tank. van Genuchten (1980) has developed a model describing the hydraulic properties of most soil types as follows:

$$\theta(h) = \begin{cases} \theta_r + \frac{\theta_s - \theta_r}{(1 + |\alpha h|)^m}, & h < 0 \\ \theta_s, & h \geq 0 \end{cases} \quad (1)$$

$$K(h) = K_s S_e^l [1 - (1 - S_e^l)^m]^2 \quad (2)$$

In Eq. (1), *h* is the soil moisture pressure head [cm], θ_s is the saturated water content [cm³/cm³], θ_r is the residual water content [cm³/cm³], and α [cm⁻¹], *m* and *n* are empirical parameters. It is required that $m = 1 - 1/n$. In Eq. (2), *K*(*h*) is the hydraulic conductivity [cm/s], *K_s* is the saturated hydraulic conductivity [cm/s], *S_e* is the effective soil moisture content given by $S_e = (\theta - \theta_r) / (\theta_s - \theta_r)$, *l* is a pore connectivity parameter with an average value of approximately 0.5 for many soils (Kandelous and Šimunek, 2010).

Soil hydraulic parameters for the sand in the sand box were estimated using a soil suction plane-table (provided by Institute of Soil Science, Chinese Academy of Sciences). A soil suction plane-table is a testing device that measures soil hydraulic parameters from soil texture and related data required by the van Genuchten–Mualem model (van Genuchten, 1980). Matlab software (Matlab 7.0, Math Works, Natick, MA) was used to obtain the four VG parameters θ_s , θ_r , α and *n* by fitting the VG model to the measured retention data. Matlab software fitted the following soil hydraulic parameters of the van Genuchten–Mualem model: $\theta_r = 0.023$ cm³/cm³, $\theta_s = 0.342$ cm³/cm³, $\alpha = 0.042$ cm⁻¹, and *n* = 5.275. The saturated hydraulic conductivity *K_s* was measured using a Guelph constant head permeameter: *K_s* = 0.495 cm/min.

The soil thermal regime was modeled with the conduction-convection heat flow equation (Sophocleous, 1979):

$$C(\theta) \frac{\partial T}{\partial t} = \frac{\partial}{\partial x} \left(\lambda_{xz}(\theta) \frac{\partial T}{\partial z} \right) - C_w q_x \frac{\partial T}{\partial x} \quad (3)$$

where *C*(θ) and *C_w* are the volumetric heat capacity of the bulk soil and

the liquid phase, respectively; λ_{xz} is the soil thermal conductivity and *q_x* for the water flux density while *T* is soil temperature. The effects of water vapor diffusion is ignored. The volumetric heat capacity *C*(θ) was determined according to De Vries (1963):

$$C(\theta) \approx (1.92\theta_n + 2.51\theta_o + 4.18\theta) \times 10^6 \quad (4)$$

where θ_n and θ_o represent the volume fractions of solid phase and organic matter in soil, respectively. The thermal conductivity as a function of soil water content can be written as (Chung and Horton, 1987):

$$\lambda(\theta) = b_1 + b_2\theta + b_3\theta^{0.5} \quad (5)$$

where *b₁*, *b₂*, *b₃* are empirical parameters that are specified for each particular soil (coarse, medium and fine texture). In this paper, the values *b₁*, *b₂*, *b₃* are HYDRUS-2D default values. The value of soil thermal parameters are shown in Table 3.

2.2.2. Initial and boundary conditions

The model domain represents a cross-section of the 2-D sand tank (Fig. 2). HYDRUS-2D uses the Galerkin finite-element method to solve the governing water flow equation and heat flow equation. The numerical solution of the transport domain using HYDRUS-2D was obtained. Domain geometry was rectangular, and measured 60 cm wide and 80 cm deep. During the low temperature water application, a constant head boundary condition was used at the location of the left infiltration boundary of 25 cm located at 55 cm below the soil surface. The infiltration line was assumed to be a line source. The remaining part of the left boundary was a zero-flux boundary during the infiltration event. A zero-flux boundary condition was also used at the bottom boundary. An atmospheric boundary was used at the soil surface and a free drainage boundary condition was used at the right boundary.

The soil heat regime was affected by water temperature. Then the constant water head boundary was used as the Cauchy type boundary condition. The Dirichlet type boundary condition was used at the soil surface. During water application, the soil surface boundary had a constant radiation temperature of 22 °C, which was controlled by the solar radiation controller system. The Neuman type boundaries were used at the remaining part of the left and right boundaries. The bottom boundary was also used the Neuman type boundary condition.

2.2.3. Model calibration

Based on the indoor test results, the numerical model was calibrated to determine the reasonable model parameter values. Experiment #1 was used as the observation data for the calibration. The parameter optimization (inverse) module incorporated in HYDRUS-2D (Šimunek

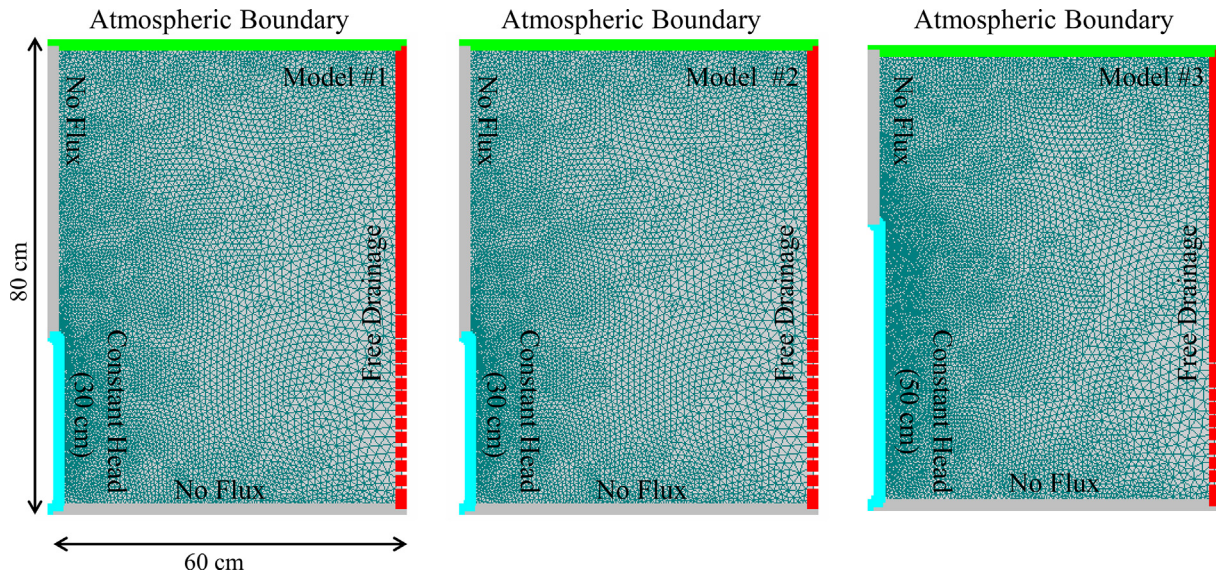


Fig. 2. Finite element mesh of modeling domain, and boundary conditions of the modeling scenarios for different experiments: (Model #1) Exp1, (Model #2) Exp2, and (Model #3) Exp3.

Table 4
Soil hydraulic parameters used in HYDRUS-2D model.

Parameter	θ_r	θ_s	α	n	K_s	l
	(cm ³ ·cm ⁻³)		(l·cm ⁻¹)		(cm·min ⁻¹)	
Initial value	0.023	0.342	0.042	5.275	0.495	0.5
Calibrated value	0.021	0.342	0.038	5.2753	0.49	0.5

Note: θ_r is residual water content, θ_s is saturated water content, α and n are empirical shape parameters, K_s is saturated hydraulic conductivity and l is pore connectivity parameter.

et al., 2006) was employed to identify θ_s , θ_r , α and n and K_s ($\theta_r = 0.021$ cm³/cm³, $\theta_s = 0.342$ cm³/cm³, $\alpha = 0.038$ cm⁻¹, $n = 5.275$ and $K_s = 0.49$ cm/min). The final calibrated value of soil hydraulic parameters are shown in Table 4.

In this paper, root-mean-square error (RMSE), coefficient of determination (R^2) and relative error (Re) were used to evaluate the simulation accuracy of the model.

The root mean square error (RMSE) of the observed and simulated sand temperature were used to provide a quantitative comparison of the goodness-of-fit between observed and simulated data, and assess the performance of the riparian zone. R^2 is the coefficient of determination between the simulated and observed values based on the $y = x$ linear regression equation. Re is the relative error between the simulated and observed values, which are defined as:

$$RMSE = \sqrt{\sum_{i=1}^n (O_i - S_i)^2 / n} \tag{6}$$

$$R^2 = 1 - \frac{\sum_{i=1}^n (O_i - S_i)^2}{\sum_{i=1}^n (O_i - \bar{O})^2} \tag{7}$$

$$Re = \sqrt{\frac{\sum_{i=1}^n (O_i - S_i)^2}{\sum_{i=1}^n O_i^2}} \tag{8}$$

where n = number of observations, S_i and O_i are the predicted and observed data, respectively, and \bar{O} is the observed mean sand temperature.

3. Results and discussion

3.1. Temperature fields

Fig. 3 shows the heat plume movement in three different experiments of the sand tank at different times (30, 60, 180, 270 and 500 min) after the low temperature water injection. Considering the solar radiation impact of riparian zone, Experiment #1 and #3 increased the soil surface radiation temperature boundary conditions of 22 °C and changed the infiltration hydraulic head conditions of 25 cm and 45 cm, respectively. Laboratory experiments simulated the temperature distribution of the sand tank which were affected by water temperature, hydraulic head and radiation.

Fig. 3 shows the patterns are obviously different for the three-different heat infiltration tests. The heat plume generally followed the direction of the groundwater flow, which is consistent with the results obtained by Klepikova et al. (2016). Contours, shaped as a '7' were observed for temperature fields in the sand tank. The phenomenon of low temperature water moving through the sand tank horizontally and vertically is evident. The temperature gradient gradually decreases in the horizontal direction. In the vertical direction the soil moisture was affected by the sand's matric suction so that the water flow moves upwards and drives the temperature to move upwards. The temperature gradient gradually increases from lower to upper sections of the sand tank. In the horizontal direction, low temperatures are evident in the inlet infiltration area and high temperatures are evident in the outlet infiltration area. At inlets, the water temperature is dominated by its inlet conditions. In the vertical direction, the temperature of upper part is higher and the temperature of the lower part is low. The area of the temperature zone changes with infiltration time, the high temperature zone decreases, and the low temperature zone increases gradually. Whether in the horizontal direction or in the vertical direction, temperature fields of sand tank can be divided into low, medium, and high temperature zones. This indicates that the sand tank temperature is significantly influenced by the low-temperature water.

Fig. 4 shows the processed data for selected sensors. After three experiments the low temperature water was injected at time $t = 0$ min, collecting 500 min of test data. Three color curves show the temperature recorded after injection of the low temperature water. B1, B2, B3, B4, B5 and B6 represent different cross section. Making cross section comparisons, the B1 section reached the steady-state in less time than the other sections (B2, B3, B4, B5, B6) and had faster descent speeds

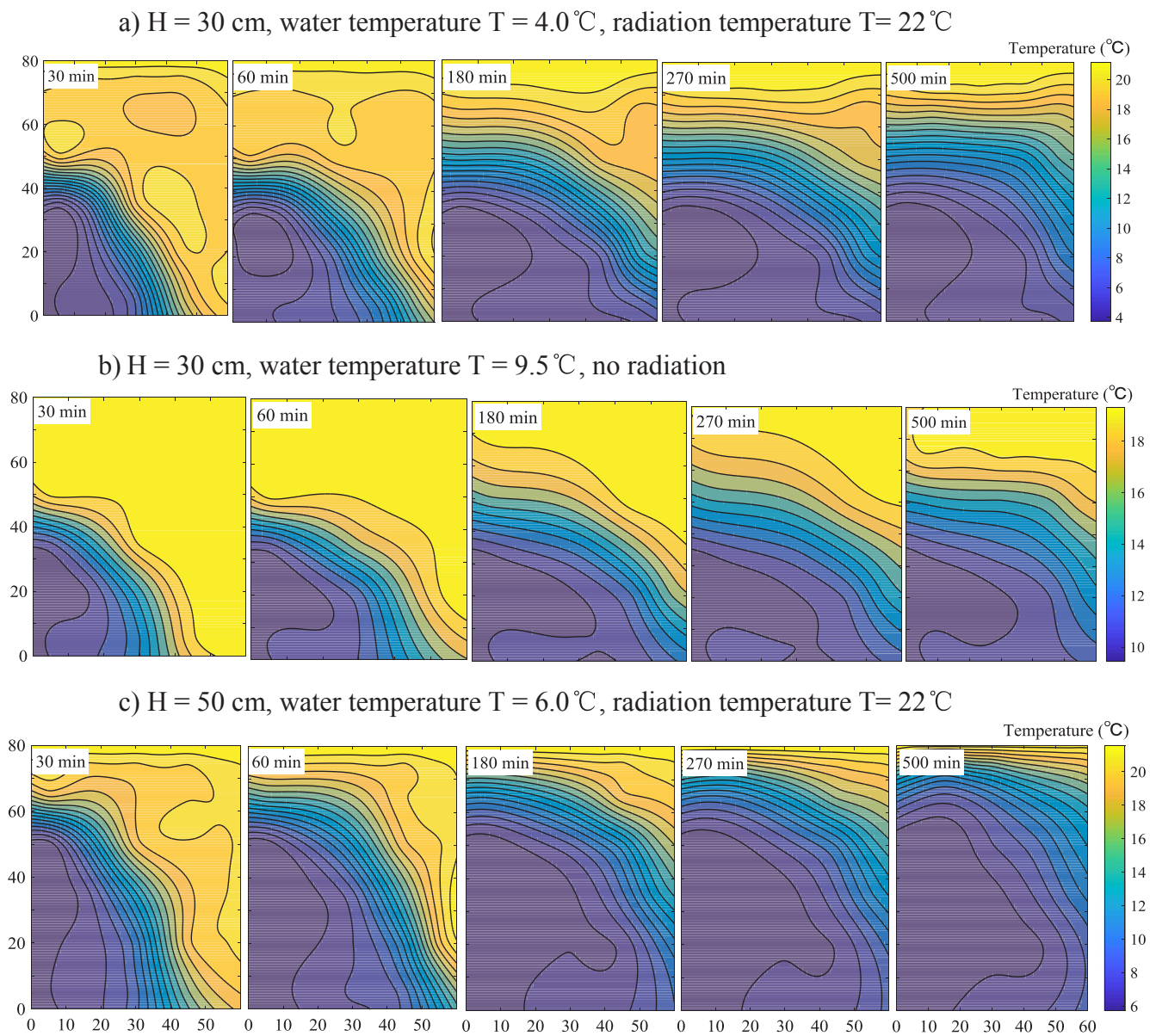


Fig. 3. Heat plume movement in three different experiments of the sand tank at different times (30, 60, 180, 270 and 500 min) after the low temperature water injection.

than other sections. Making vertical section comparison, A1 (T1, T11 and T16) and A2 (T7) sections indicate that the nearer the temperature observation point was to the infiltration boundary, the lower the temperature of the observation point and the time required to reach the steady state, and the higher the rate of temperature reduction. The influence of the upstream water temperature on the temperature field of the sand tank is mainly reflected in the A1, A2 and A3 sections. Changes in infiltration water temperature are only evident in temperature values taken in sections A1, A2 and A3.

As can be seen from Fig. 4, the influence of the hydraulic head on the temperature field was mainly reflected in A3, A4 and A5 sections. Increasing hydraulic head increases the rate at which temperatures decrease and the total amount of temperature change. Data indicated that the higher the hydraulic head, the shorter the time for the temperature drop and the greater the range of temperature decreases. From the temperature monitoring data of the three sections (B4, B5 and B6), it can be seen that the infiltration temperature value of Experiment #3 (6.0 °C) is between Experiment #1 (4.0 °C) and #2 (9.5 °C). But the rate of temperature reduction and total time of Experiment #3 was faster

than those in Experiments #1 and #2. Clearly, the influence of hydraulic head on the temperature field was greater than that of water temperature and radiation. It can be seen from the B6 section that the radiation temperature has a certain effect on the surface temperature of the sand tank. The higher the radiation temperature was, the higher the surface temperature. As can be seen from Experiment #1, the surface temperature of the sand tank gradually increased with time and approaches the radiation temperature. Experiment #2 was not affected by the radiation temperature, the surface temperature changed very little. The surface temperature of Experiment #3 increased before 100 min, and then decreased gradually with the influence of low temperature water infiltration.

Fig. 5 shows that the time-series record of temperature sensor in sand tank. Temperature time series measurements were taken at six horizontal locations B1, B2, B3, B4, B5 and B6 (bottom to top rows), with each location composed of five temperature sensors. The effect of the water temperature on the sand tank temperature field was obvious. With the passage of time, the temperature values of different parts of the sand tank have changed through low temperature water, and the

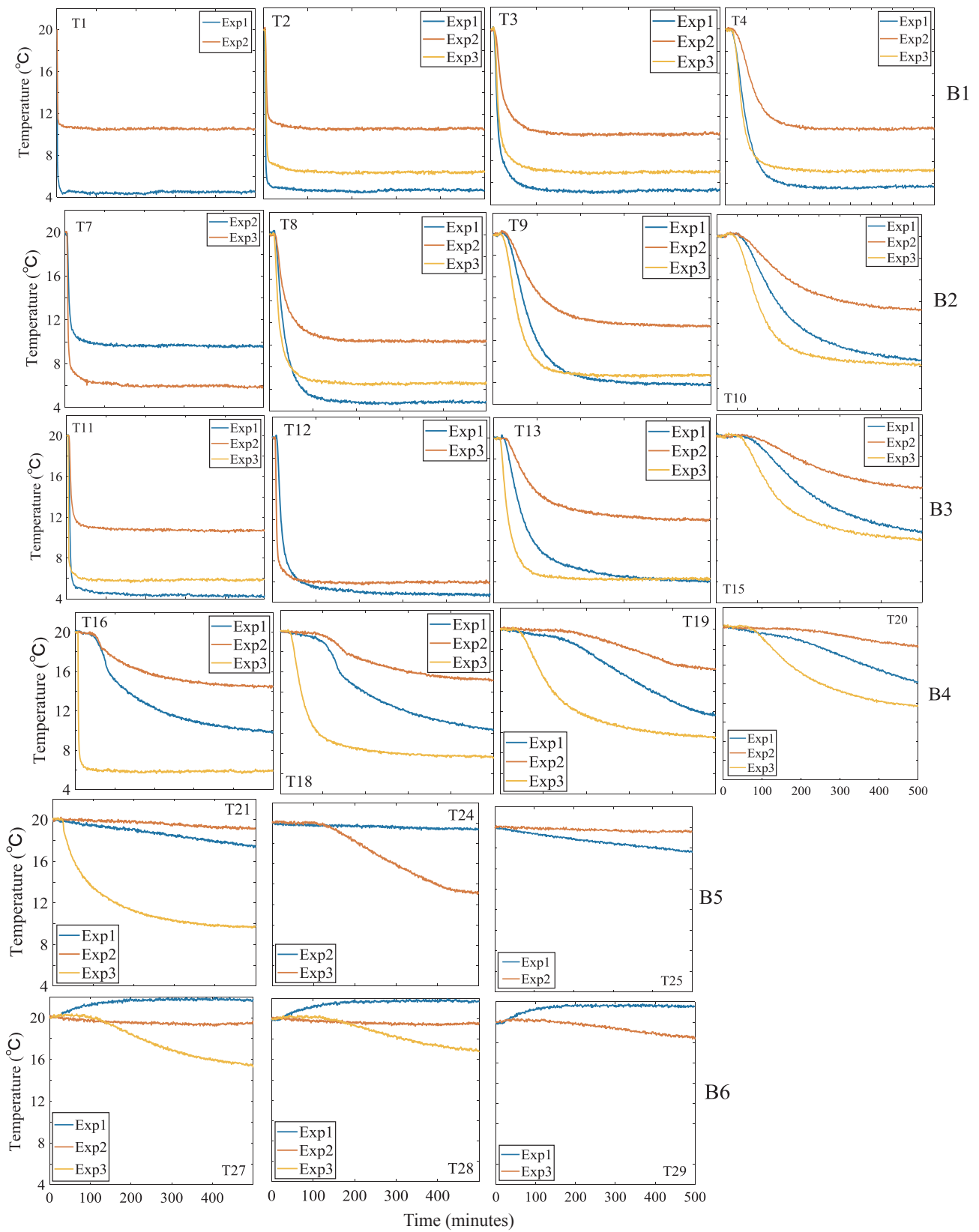


Fig. 4. Processed data for selected sensors. After three experiments the low temperature water was injected at time $t = 0$ min, collecting 500 min of test data. Three color curves show the temperature recorded after injection of the low temperature water. B1, B2, B3, B4, B5 and B6 represent different cross sections, respectively.

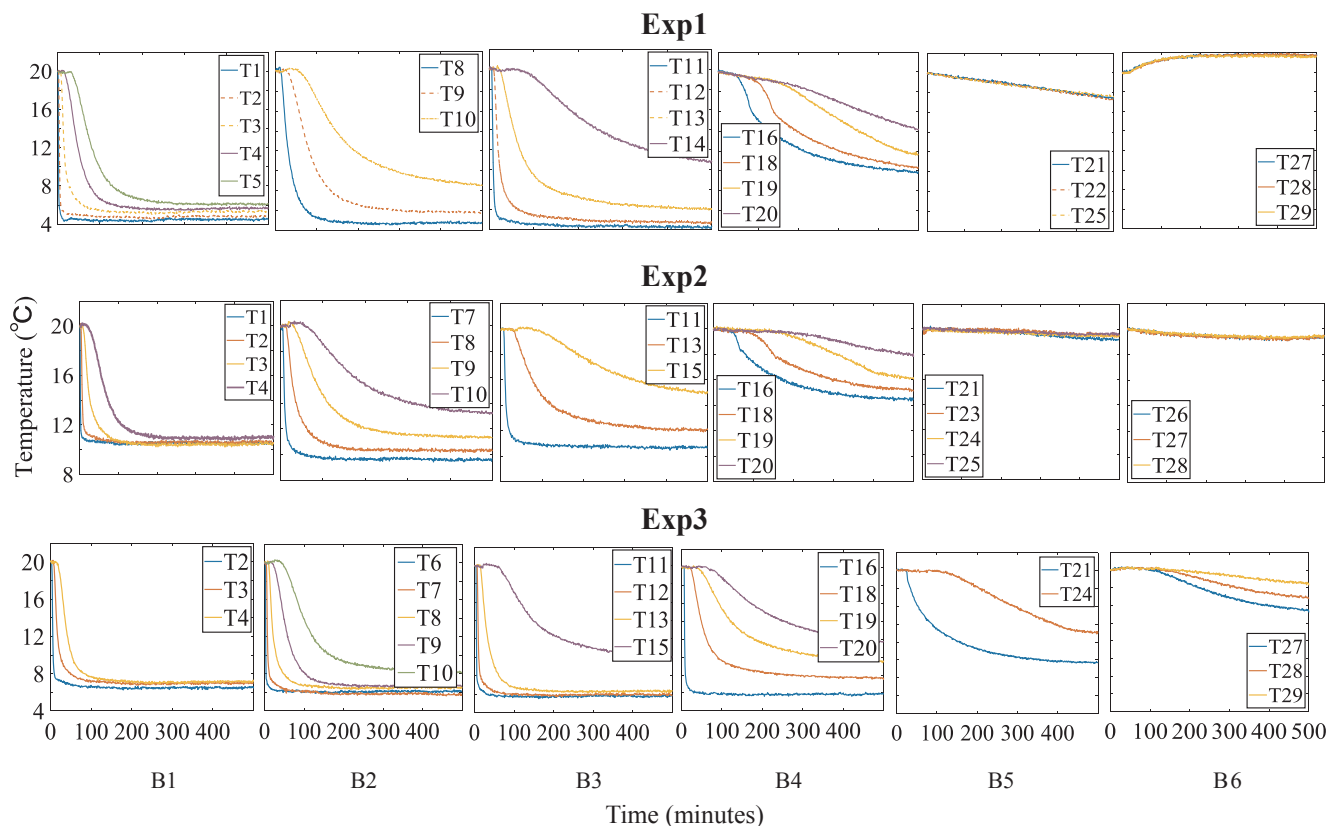


Fig. 5. Time-series record of temperature sensor in sand tank. Temperature time series at six horizontal locations B1, B2, B3, B4, B5 and B6 (bottom to top rows), with each location composed of five temperature sensors.

variation is very similar. In the B1 section, the temperature reaches the steady state in less time than the other sections, the rate of temperature reduction was faster than observed in the other sections. Sand tank temperatures measured in Experiment # 1 and Experiment # 3 were affected by the infiltration water temperature of upstream reservoir and soil surface radiation. The temperature of every section from B1 to B5 is greatly influenced by low temperature water, and the temperature at each observation point gradually decreases, indicating that the infiltration water temperature had a significant impact on the time series temperatures measured in these five sections.

As time goes on, the temperature of section B6 gradually increased, approaching the radiation temperature of 22 °C in Experiment #1. In the first 100 min, the temperature of section B6 gradually increased and the later decreased gradually in Experiment #3, indicating that infiltration water temperature and surface radiation temperature were dominant factors concurrently, and had the greater impact on the B6 section. It can also be seen from Fig. 5 that under conditions of increasing hydraulic head upstream, the more obvious the influence of the temperature field which was observed in the sand tank. When the hydraulic head is 45 cm, it can affect the temperature field of the entire sand tank, but at hydraulic head of 25 cm, the effects of temperature on the B5 and B6 sections were much less.

The sand water temperature gradient was the ratio of the difference in soil temperature to the distance in a certain direction between two points in the sand. For example, (A4-T29) – (A3-T28) represented the ratio of temperature difference and horizontal straight-line distance between T29 and T28 at a distance of 15 cm and depth of 5 cm. The ratio of (A3-T28) – (A3-T18) represented the temperature difference and vertical straight-line distance between T28 and T18 at the distance of 25 cm and the depth of 5 cm and 30 cm. Fig. 6 shows comparisons of sand water temperature gradients between two directions during Experiment # 3. One is the horizontal direction parallel to the sand

surface (e.g., (A4-T29) – (A3-T28)) and the other is the direction vertical to the sand surface (e.g., (A3-T28) – (A3-T18)). Fig. 6 shows that sand water temperature gradients fluctuate greatly in the horizontal and vertical direction, especially at deeper sand layers. This is mainly due to the influence of water gravity and sand matrix suction. First, When the upstream flow infiltrates the sand tank, the bottom sand layer is more easily saturated. It can be seen from Fig. 6 that the influence of the lateral water flow on the temperature gradient changes in both the horizontal and vertical directions. The horizontal temperature gradient gradually decreases, and the vertical temperature gradient gradually increases. During the initial stage of infiltration, the temperature gradient in the horizontal direction is larger than the temperature gradient in the vertical direction. Over time, the temperature gradient in the vertical direction exceeds the temperature gradient in the horizontal direction. The horizontal temperature gradient of the top sand layer is less affected by the water temperature.

Fig. 6 shows that, at the depth of 60 cm ((A4 – T9) – (A3 – T8)), the maximum temperature gradient value in the horizontal direction is 0.59 °C/cm and the maximum time is 30 min, which is larger and faster than that at the depth of 45 cm, 30 cm and 5 cm, respectively. The temperature gradient of 45 cm, 30 cm and 5 cm in the horizontal direction is 0.48 °C/cm, 0.38 °C/cm and less than 0.20 °C/cm and the maximum time is 67 min, 85 min and more than 300 min, respectively. In contrast, the maximum temperature gradient value in the vertical direction ((A3 – T8) – (A3 – T3)) is 0.20 °C/cm and the maximum time is 14 min, which is shorter and faster than other vertical direction ((A3-T13)-(A3-T8)), ((A3-T18)-(A3-T13)) and ((A3-T28)-(A3-T18)), respectively. The temperature gradient in the vertical direction ((A3-T13)-(A3-T8)), ((A3-T18)-(A3-T13)) and ((A3-T28)-(A3-T18)) is 0.32 °C/cm, 0.38 °C/cm and 0.45 °C/cm, and the maximum time is 20 min, 33 min and 122 min, respectively. As can also be seen from Fig. 6, the horizontal temperature gradient is more affected than the vertical direction

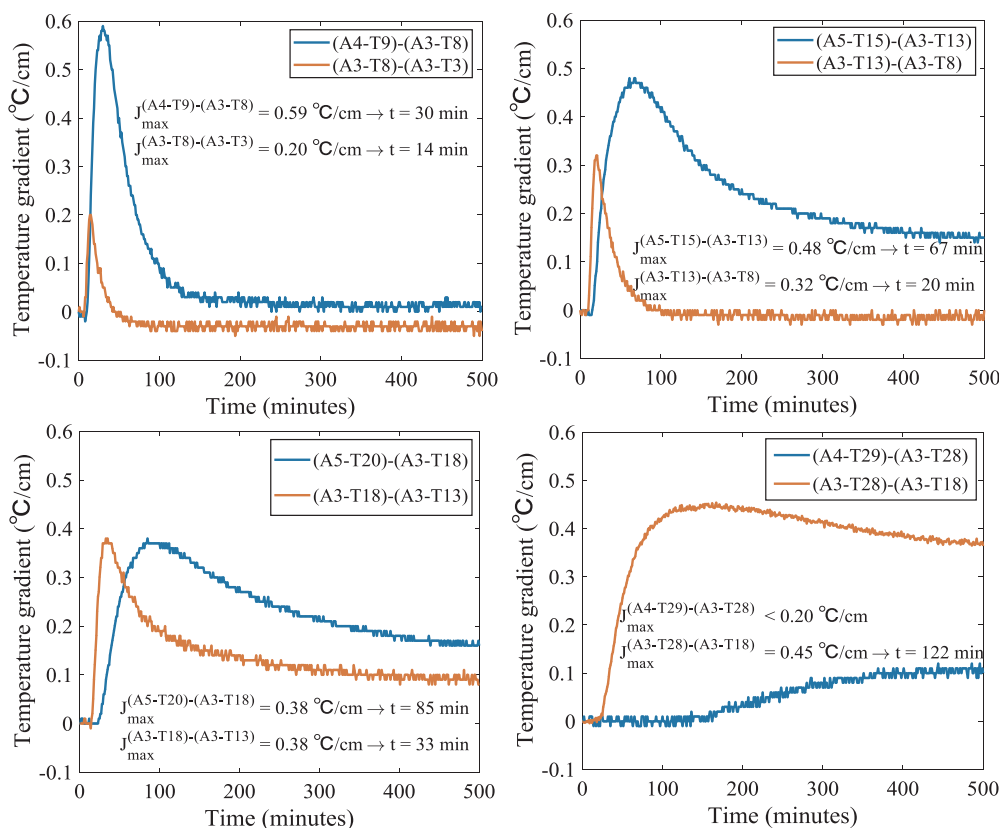


Fig. 6. Comparisons of temperature gradients in different directions of Experiment #3.

by lateral water flow. The vertical direction temperature gradient is affected by both water flow and the sand substrate suction, and the temperature gradient gradually increases.

3.2. Analysis of the temperature difference curves

The evolution of the temperature measured in these selected observation points (T1, T2, T3, T4, T6, T7, T8, T9, T11, T12, T13, T15, T16, T18, T19 and T20) is presented in Fig. 7.

The comparison between temperature difference curves in the Experiment #1, Experiment #2 and Experiment #3 clearly shows that heat pulse travels fastest in the high hydraulic head (Experiment #3). The temperature difference curves are also characterized by longer tailings. The shape is consistent with the results obtained by Wildemeersch et al. (2014). Maximum temperature changes were observed at these temperature sensors T1, T6, T11 and T16 after the beginning of the infiltration of low-temperature water. The four temperature observations are closest to the infiltration boundary, which are 5 cm from the infiltration boundary. Fig. 7 shows that the temperature difference values of the same horizontal section gradually decreases from left to right, sharper decrease is observed where the location is closer to the infiltration boundary. The maximum temperature variation value of high hydraulic head (Experiment #3) is 9.6 °C. This observation point was T6, which was measured 3 min after the beginning of the infiltration of low-temperature water. The observation point is 5 cm from the infiltration boundary and 20 cm from the bottom boundary. When the hydraulic head is low, the maximum temperature variation value is 11.44 °C (Experiment #1). This observation point was made 2 min after the beginning of the infiltration of low-temperature water and in the temperature sensor T1. The observation point is 5 cm from the infiltration boundary and 5 cm from the bottom boundary. It can be seen from the observation point T1 that although infiltration hydraulic head in Experiment #1 and #2 is the same, but 4 °C of the

infiltration water temperature of Experiment #1 is lower than 9.5 °C of Experiment #2, in order to reduce 20 °C of the initial temperature, the temperature drop is faster and the temperature difference value is bigger. From the observation point T11, it can be seen that the higher the infiltration water head, faster temperature drops, and greater temperature differences were observed.

3.3. Model validation

Fig. 8 shows the temporal variation of measured and simulated temperatures for selected sensors during three different experiments. Root-mean-square error (RMSE), coefficient of determination (R^2) and relative error (Re) were used to evaluate the simulation accuracy of the model. The results are shown in Table 5. It can be seen from Table 5 that the RMSE of Experiment #1 (except T10) ranges from 0.29 °C to 2.53 °C, the average is 1.12 °C, the fitting effect is good. The RMSE of T10 observation point is 4.73 °C and the error is large. Relevance can be expressed by a coefficient of determination (R^2). Correlated observation points accounted for 81.8% ($R^2 > 0.6$). Among them, the highly relevant observation points accounted for 63.6% ($R^2 > 0.8$). Relative error (Re) mostly is less than 10%. The Re value of observation point T2, T3, T11, T12 is large, the fitting is not accurate.

The previous calibrated model was further validated by using Experiment #2 and #3. The results are shown in Figs. 9 and 10. The agreement of the results is also indicated by the low values of RMSE, R^2 and Re, as those listed in Table 5. The RMSE of Experiment #2 ranges from 0.27 °C to 2.24 °C with an average value of 0.77 °C, which shows good agreement. The correlation coefficient R^2 of the temperature observation points T20, T21, T23, T24, T27 and T28 are less than 0, it shows that there is a great deviation between the simulated values and the experimental values. The R^2 of other observation points are within a reasonable range. The relative error Re are less than 10% except observation point T10 in Experiment #2. RMSE of Experiment #3 ranges

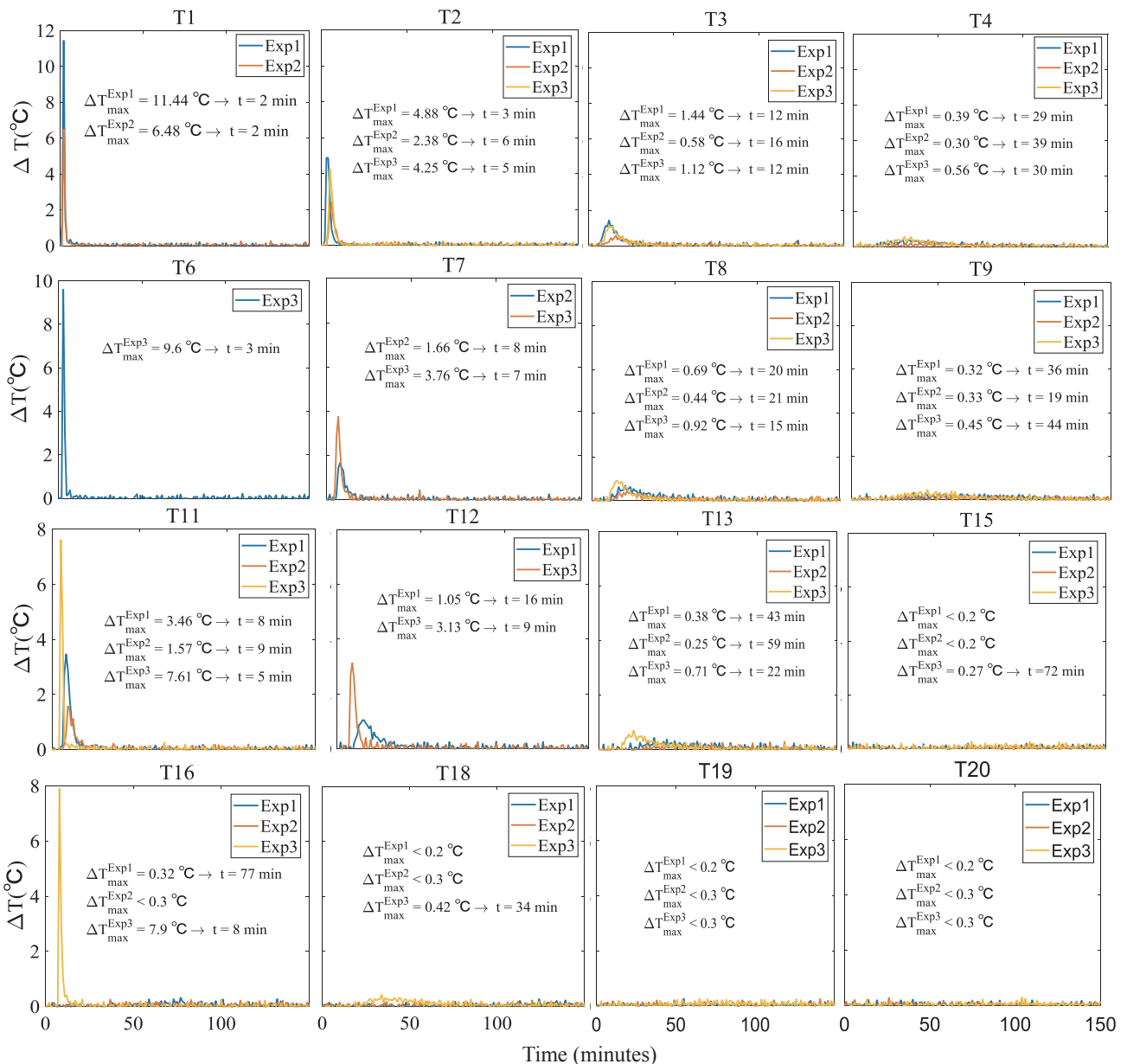


Fig. 7. Temperature difference curves measured in selected sensors.

from 0.36 °C to 2.83 °C, the average is 1.1 °C, and the fitting effect is good. R^2 is the range of -0.12 to 0.98 , where $R^2 > 0.6$ accounts for 85.7%. The experimental value agrees well with the simulated value. The Re value of T10, T11, T12, T15 and T16 is large, and other temperature observation point value within a reasonable range.

Fig. 11 shows the temporal variation at different depths in vertical direction (Length = 30 cm) of three experiments. The soil temperature profile shows two stages of the infiltration, which can clearly reveal the temperature variation as infiltration proceeds. The low-temperature forward movement process was the first stage (0–180 min). In the first 30 min, soil temperature did not change with time below the surface of 35 cm. Soil temperature gradually decreased with the infiltration time in the depth range of 35–80 cm. The temperature of the soil below hydraulic head was close to the infiltration water temperature when the infiltration time reached 180 min (Fig. 11a, b). With increases in the hydraulic head (Fig. 11c), in the first 30 min, the temperature of surface soil also changed with the infiltration time. The temperature of the soil below the infiltration hydraulic head is close to the infiltration water temperature during the 60 min and 180 min time period (Fig. 11c). At

the second stage (180–500 min), the temperature profile gradually migrated to the left, the temperature of the soil above the infiltration hydraulic head decreased gradually to close to the infiltration water temperature, and the low temperature region increased gradually. Because of the influence of the high hydraulic head, the low temperature area is larger than the low head. It can be seen from Fig. 11c (0–60 min) that there was a clear trend in temperature fluctuation observed in which temperature increases first and then decreases, and subsequently decreased gradually. This is the reason that the temperature of the soil surface (0–10 cm) is affected by the surface radiation. For the different depth profiles on the fitting consistency, it was evaluated through RMSE, R^2 and Re, and the results are shown in Table 6. For RMSE, the variation range of Experiment #1 is between 1.1 and 1.82 °C and the average is 1.49 °C. The variation range of Experiment #2 is 0.31–0.89 °C and the average is 0.59 °C. The variation range of Experiment #3 is 0.68–1.34 °C, the average is 1.01 °C. For R^2 , the R^2 of three conditions is greater than 0.87, and therefore reflects a very strong correlation. For Re, the value of Experiment #1 and Experiment #3 is large which is about 10%, the Re of Experiment #2 is very small,

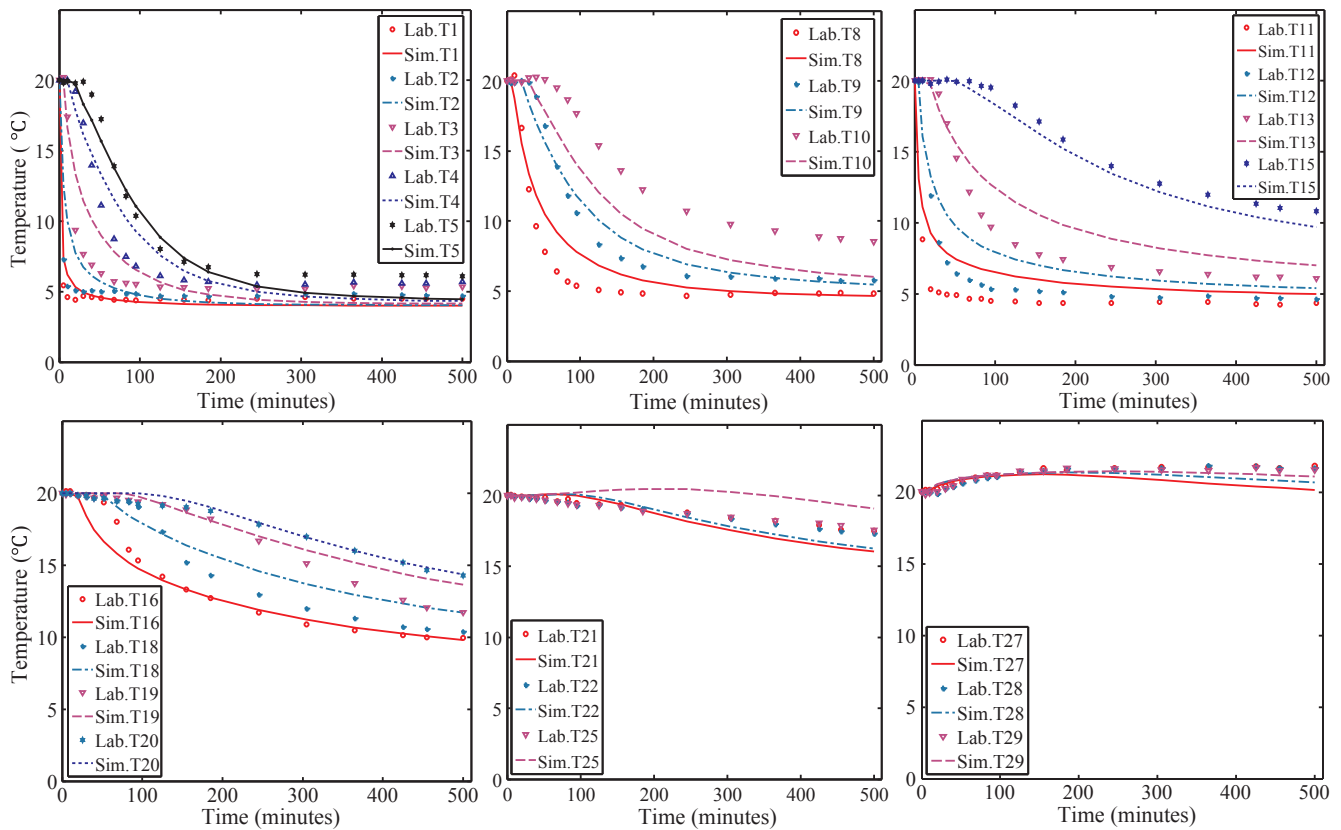


Fig. 8. Temporal variation of measured and simulated temperatures for selected sensors during Experiment #1.

Table 5

The root mean squared error (RMSE), determination coefficient (R^2) and relative error (Re) for sand temperature during calibration (Experiment #1) and validation (Experiment #2 and Experiment #3).

	Temperature sensor	RMSE (°C)	R^2	Re	Temperature sensor	RMSE (°C)	R^2	Re	
Experiment #1	T1	0.69	0.96	10.78%	T15	0.65	0.97	3.75%	
	T2	1.83	0.71	27.21%	T16	1.05	0.93	6.60%	
	T3	1.83	0.87	19.40%	T18	1.03	0.93	6.15%	
	T4	1.43	0.94	12.11%	T19	0.89	0.91	4.96%	
	T5	1.09	0.97	8.06%	T20	0.35	0.97	1.91%	
	T8	1.52	0.93	14.38%	T21	0.70	0.30	3.63%	
	T9	0.94	0.98	6.94%	T22	0.55	0.61	2.86%	
	T10	4.73	0.74	14.96%	T25	1.11	-1.14	5.79%	
	T11	2.53	0.72	31.59%	T27	0.72	-0.21	3.39%	
	T12	2.13	0.84	21.77%	T28	0.51	0.48	2.43%	
	T13	1.74	0.90	13.26%	T29	0.29	0.81	1.39%	
	Experiment #2	T1	0.82	0.84	7.27%	T16	0.97	0.80	5.53%
		T2	0.98	0.84	8.25%	T18	0.37	0.96	2.01%
T3		0.80	0.94	6.15%	T19	0.41	0.92	2.12%	
T4		0.92	0.94	6.21%	T20	0.82	-0.47	4.19%	
T7		1.09	0.88	9.51%	T21	1.09	-12.76	5.52%	
T8		0.73	0.96	5.43%	T23	0.73	-17.27	3.70%	
T9		0.82	0.95	5.19%	T24	0.38	-3.72	1.91%	
T10		2.24	0.32	12.63%	T25	0.29	-1.97	1.44%	
T11		1.22	0.82	9.81%	T26	0.19	0.50	0.94%	
T13		0.51	0.98	3.19%	T27	0.24	-0.04	1.20%	
T15		1.03	0.71	5.57%	T28	0.27	-0.61	1.38%	
Experiment #3		T2	0.82	0.94	9.75%	T15	2.35	0.67	14.25%
		T3	1.22	0.92	11.78%	T16	1.06	0.88	14.60%
	T4	1.08	0.95	9.14%	T18	1.27	0.93	9.68%	
	T6	0.36	0.99	4.84%	T19	0.66	0.98	4.14%	
	T7	0.61	0.96	8.03%	T20	0.58	0.97	3.29%	
	T8	0.76	0.97	8.05%	T21	1.25	0.89	8.43%	
	T9	1.03	0.96	8.14%	T24	0.77	0.91	4.15%	
	T10	2.83	0.68	18.67%	T27	1.32	0.44	6.96%	
	T11	0.84	0.94	10.88%	T28	0.86	0.47	4.45%	
	T12	1.56	0.97	17.56%	T29	0.75	-0.12	3.79%	
	T13	1.17	0.95	10.61%					

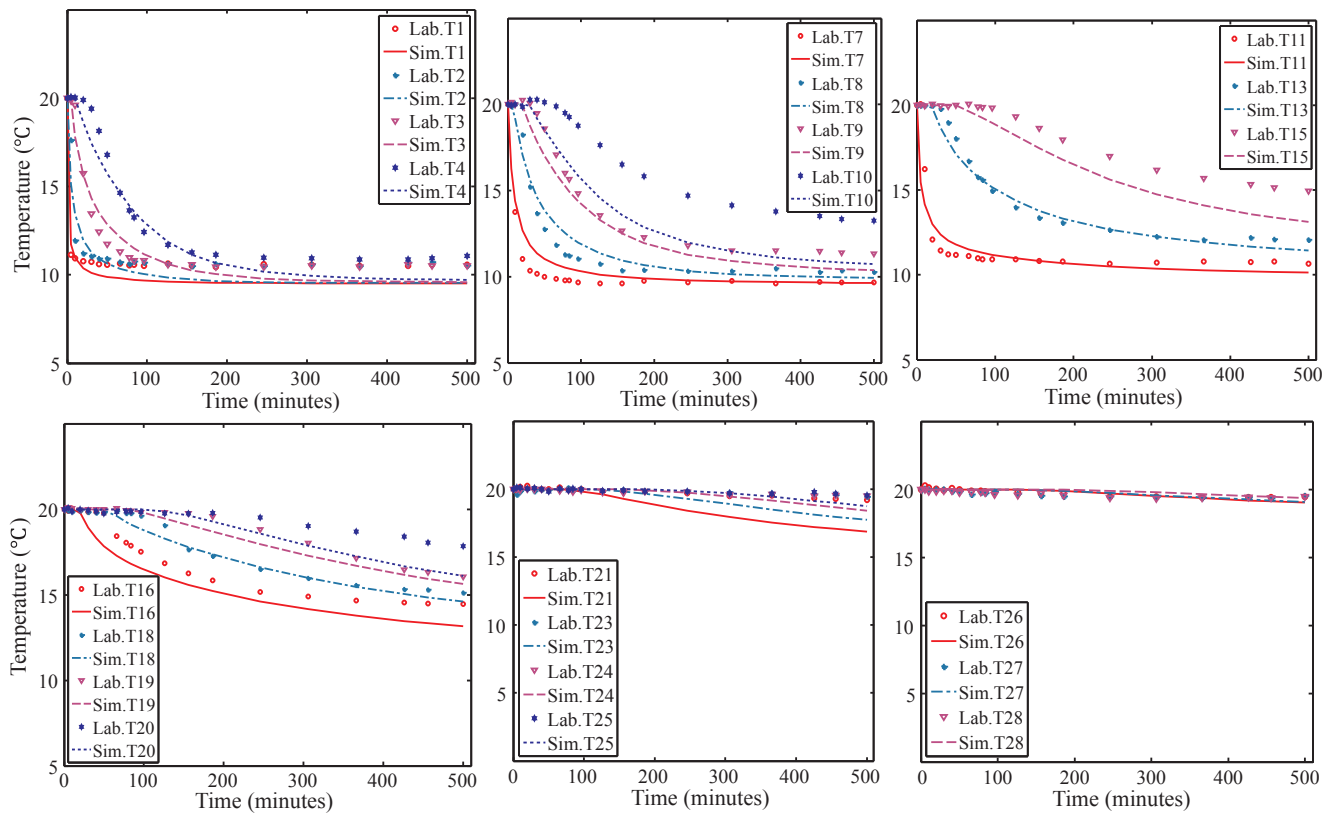


Fig. 9. Temporal variation of measured and simulated temperatures for selected sensors during Experiment #2.

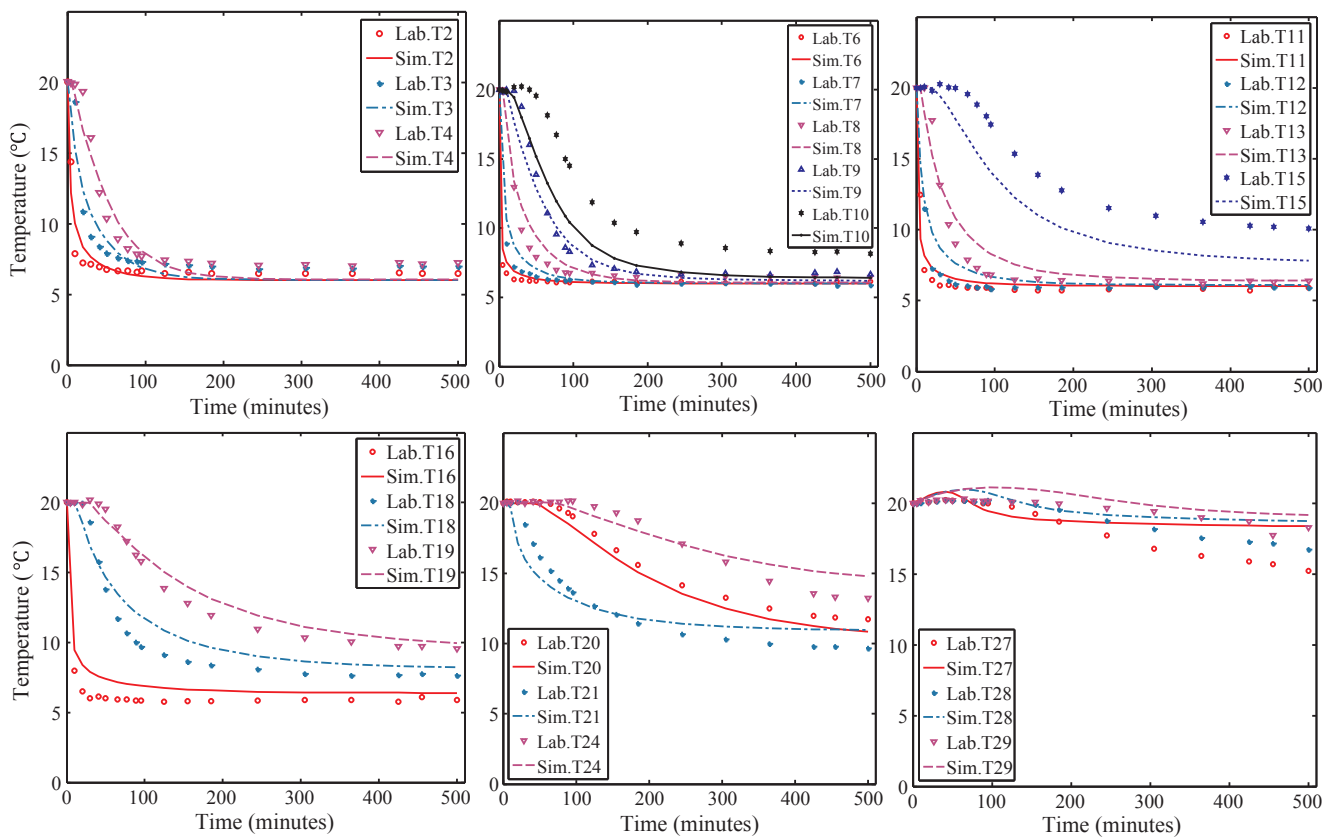


Fig. 10. Temporal variation of measured and simulated temperatures for selected sensors during Experiment #3.

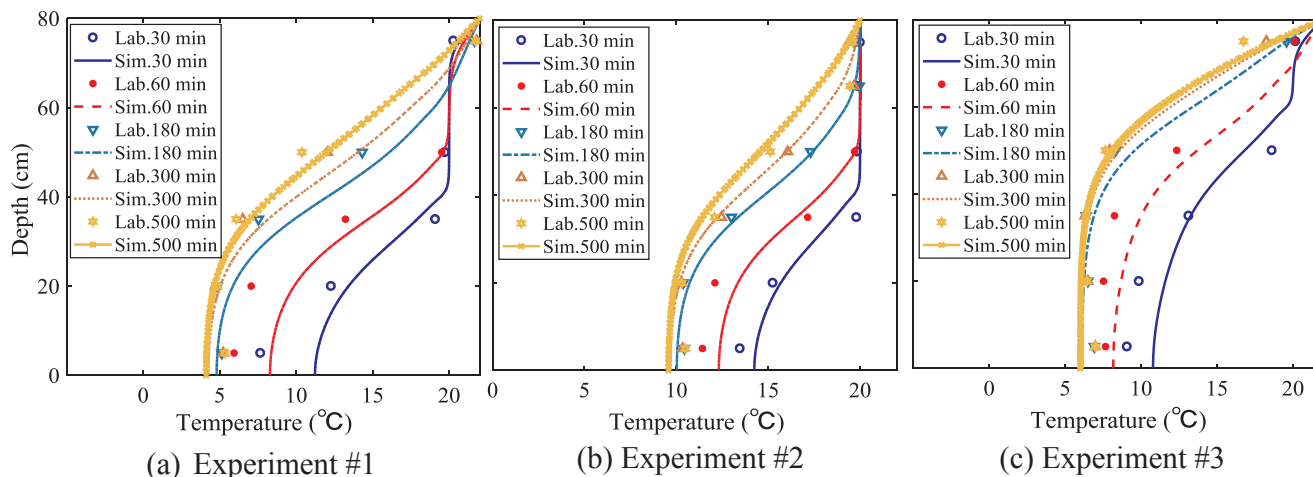


Fig. 11. Temporal variation at different depths in vertical direction (Length = 30 cm) of three experiments.

Table 6

The root mean squared error (RMSE), determination coefficient (R^2) and relative error (Re) for sand tank vertical profile (Length = 30 cm) temperature during calibration (Experiment #1) and validation (Experiment #2 and Experiment #3).

	Times	RMSE (°C)	R^2	Re
Experiment #1	30 min	1.82	0.87	11.00%
	60 min	1.79	0.92	12.19%
	180 min	1.43	0.95	11.46%
	300 min	1.29	0.96	10.83%
	500 min	1.1	0.97	9.54%
Experiment #2	30 min	0.62	0.95	0.11%
	60 min	0.68	0.96	0.16%
	180 min	0.31	0.99	0.04%
	300 min	0.44	0.99	0.08%
	500 min	0.89	0.95	0.35%
Experiment #3	30 min	1.34	0.91	8.99%
	60 min	1.21	0.94	9.95%
	180 min	0.76	0.98	7.06%
	300 min	0.68	0.98	6.67%
	500 min	1.05	0.93	10.84%

which has very high fitting consistency.

3.4. Sensitivity analysis

3.4.1. Local sensitivity analysis method

The local sensitivity analysis fluctuates slightly near the best estimate of a parameter. The rate of change of the model result is calculated by changing the parameter in the very small range under the condition that the other parameters are kept constant. The sensitivity analysis is performed to determine the main influencing factors that affect the output of the model, thus contributing to better prediction of the model.

In the paper, the Experiment #1 as the analysis object was selected. The sensitivity was analyzed based on the seven parameters: hydraulic head (H), infiltration water temperature (T), the saturated hydraulic conductivity (K_s), Van Genuchten parameters n and α , residual moisture content (θ_r), and saturated moisture content (θ_s). The input parameters were varied $\pm 10\%$, $\pm 15\%$ and $\pm 20\%$ of their baseline values. In each running model, each step changed only one input parameter, and the remaining parameters stayed unchanged. As the physical units are not the same, so the evaluation of indicators should be reunified. In this paper, the ratio between the difference of initial and changed values, and initial value (expressed in percentage) is calculated to check the local sensitivity analyses.

Due to the spatial nature of the numerical model, the vertical section of $x = 30$ cm was selected as the research object, the varying temperature field distribution of each parameter was obtained by numerical simulations, and then subtractions were made at each observation point between the varying temperature field and the rated temperature field and the difference of each observation point was averaged to describe temperature changes. The time period was selected as 0–500 min. The results of main input parameters are shown in Fig. 12. If the parameter change has little effect on the model, it indicates the model is not sensitive to the factor, and on the contrary, it is sensitive.

Fig. 12 shows that when the hydraulic head H fluctuates 20% and -20% , the temperature field fluctuates by about -11.87% and 10.08% , respectively. When the infiltration water temperature T fluctuates 20% and -20% , the temperature field fluctuates about both 3.17% . When the saturated hydraulic conductivity K_s fluctuates 20% and -20% , the temperature field fluctuates about -5.63% and 4.5% , respectively. When the α fluctuates by 20% and -20% , the temperature field fluctuates by about 5.96% and -7.94% , respectively. Temperature fluctuations caused by other parameters averaged about 1%. Though the variation degree varied, it is apparent that the model is most sensitive to hydraulic head (H), followed by Van Genuchten parameter α , permeability coefficient (K_s), water temperature (T), Van Genuchten parameter n , residual moisture content (θ_r), saturated moisture content (θ_s).

The variation of each parameter is linear with the change of temperature field. The parameters positively which are related to the temperature field are T , α , θ_r and θ_s , which means the parameter value becomes larger, the temperature becomes larger, and vice versa. The parameters which are negatively related to the temperature field are H , K_s and n , and the results are consistent with the qualitative analysis.

3.4.2. Global sensitivity analysis method

The local sensitivity analysis can only analyze one parameter at a time. The interaction influence could not be considered between the parameters on the model. Therefore, the global sensitivity analysis was made. The Morris method assumes that k parameters are included in the numerical model. The number of sampling points for each parameter is p . The m parameters take values at p sampling points, respectively. The vector $\mathbf{X} = [x_1, x_2, \dots, x_k]$ was gotten. Then $m \times k$ ($m = k + 1$) order matrix \mathbf{B} is (Morris, 1991):

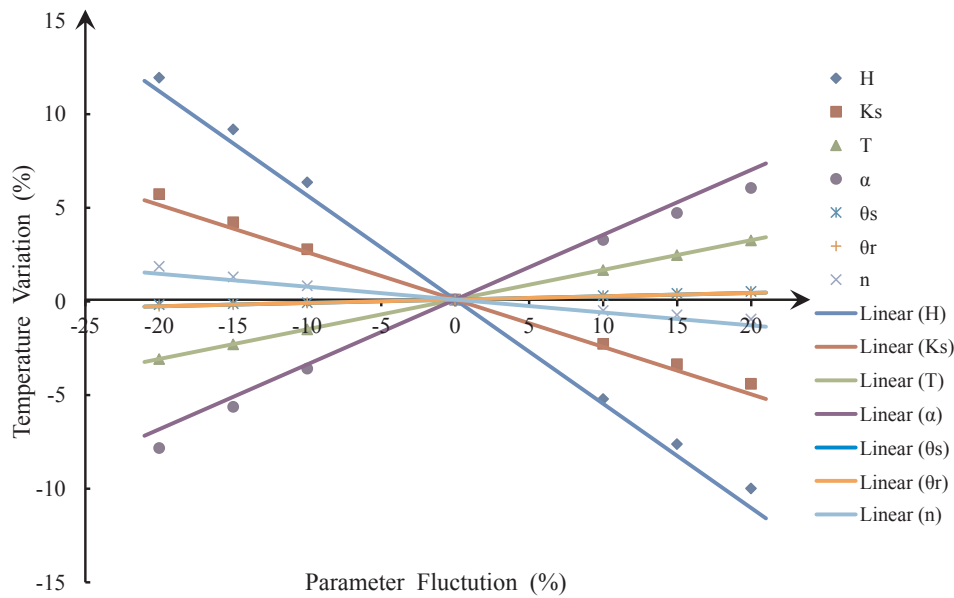


Fig. 12. The relationship between parameter fluctuation and model result.

Table 7
Temperature variation based on globe sensitivity analysis method (%).

Group	Parameter combination	Temperature Variation (%)	Group	Parameter combination	Temperature Variation (%)
1	H	-5.30	15	K _s , T, α	2.51
2	K _s	-2.55	16	T, α, θ _s	5.42
3	T	1.94	17	α, θ _s , θ _r	3.59
4	α	3.20	18	θ _s , θ _r , n	-0.16
5	θ _s	0.21	19	H, K _s , T, α	-2.94
6	θ _r	0.17	20	K _s , T, α, θ _s	2.72
7	n	-0.54	21	T, α, θ _s , θ _r	5.61
8	H, K _s	-7.70	22	α, θ _s , θ _r , n	3.03
9	K _s , T	-0.67	23	H, K _s , T, α, θ _s	-2.74
10	T, α	5.20	24	K _s , T, α, θ _s , θ _r	2.90
11	α, θ _s	3.41	25	T, α, θ _s , θ _r , n	5.03
12	θ _s , θ _r	0.38	26	H, K _s , T, α, θ _s , θ _r	-2.57
13	θ _s , n	-0.37	27	K _s , T, α, θ _s , θ _r , n	2.34
14	H, K _s , T	-5.93	28	H, K _s , T, α, θ _s , θ _r , n	-3.09

$$B = \begin{bmatrix} 0 & 0 & 0 & 0 & 0 \\ 1 & 0 & 0 & \dots & 0 \\ 1 & 1 & 0 & \dots & 0 \\ 1 & 1 & 1 & \dots & 0 \\ \dots & \dots & \dots & \dots & \dots \\ 1 & 1 & 1 & \dots & 1 \end{bmatrix} \tag{9}$$

The value 1 and 0 indicate whether the parameter is changed or not. According to the parameter arrangement, the results of global sensitivity of 28 combinations of parameters were obtained and presented in Table 7. A bar chart was used to reflect ranges of measured temperature fields for various combinations (Fig. 13). The temperature of the groups of 8, 14, 19, 23, 26, and 29 decreases significantly, they all contain the H parameter. The hydraulic head H is an important factor affecting the temperature field. Two parameters H and K_s are negatively correlated with the temperature field. They have obvious effect on the temperature field. Two parameters T and α are positively correlated with the temperature field, which suggest the temperature field variation can also be significant. Other three parameters θ_s, θ_r, and n have little effect on the temperature field.

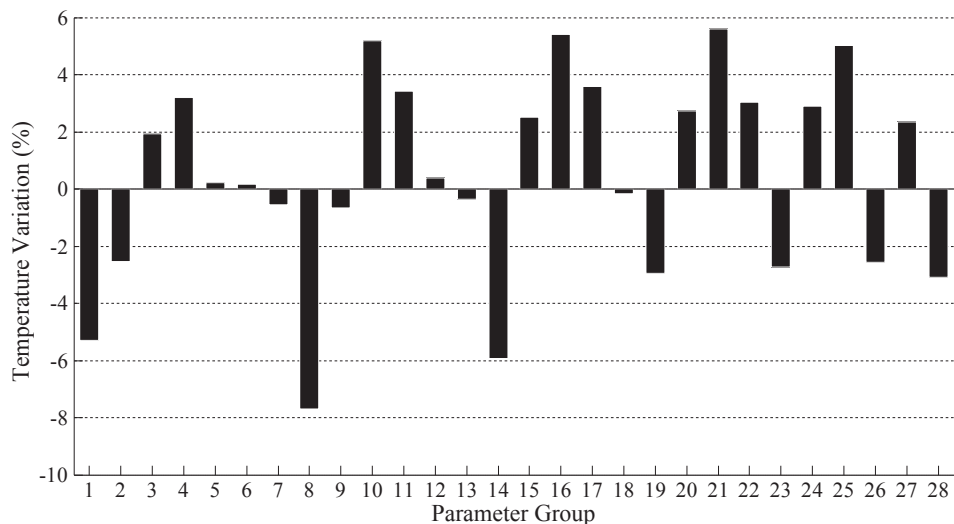


Fig. 13. Temperature variation based on globe sensitivity analysis method.

4. Conclusions

In our previous study (Ren et al., 2014), the relationship between the water temperature and bulk density and hydraulic conductivity was evaluated by low-temperature water infiltration tests on three kinds of sand column samples. A detailed temperature measurement and analysis of the two-dimensional sand tank were made. The two-dimensional sand tank was divided into six cross-sections and five longitudinal sections. Thirty temperature sensors were evenly spaced and used to monitor real-time changes in the temperature field of the sand tank under the influence of water temperature, water level and radiation.

Through the temperature field cloud diagram of the test, low-temperature water performs the phenomenon of distant diffusion on vertical upward and horizontal to the right direction. The temperature gradient gradually decreases in the horizontal direction and gradually increases from lower to upper in the vertical direction. There is low temperature zone at inlet infiltration area and high temperature zone at outlet infiltration area in the horizontal direction. From left to right the zone was divided into low temperature, medium temperature and high temperature zones. From the vertical direction of the diagram, the temperature ranges from high to low, in the upper portion and lower portion, respectively. The area of the temperature zone changed with infiltration time.

Through the study of temperature gradient of 2-D sand tank, temperature fluctuations increase with the depth of the sand layer. This is mainly due to the influence of water gravity and sand matrix suction. When the upstream water flow infiltrates the sand tank, the bottom of the sand layer is more likely to reach saturation. In both the horizontal and vertical directions, the temperature gradient clearly affects lateral flow. The temperature gradient in the horizontal direction gradually decreases, and the vertical temperature gradient gradually increases. At the initial stage of infiltration, the temperature gradient in the horizontal direction is larger than the vertical direction. At later stages of infiltration, the temperature gradient in the vertical direction is larger than in the horizontal direction. The horizontal temperature gradient of the top sand layer is less affected by the water temperature.

Through the thermal trace test, the variation of the temperature difference of the three tests is obtained. The temperature difference decreases gradually from left to right in the same horizontal section. The closer to the infiltration boundary temperature section, the greater the temperature difference changes, the faster the decline. As the infiltration hydraulic head increases, the temperature drops more rapidly and temperature differences are greater. In addition, the numerical model is evaluated by root-mean-square error (RMSE), coefficient of determination (R^2) and relative error (Re), and its results are good. The calibrated numerical model can better reflect the dynamic variation of temperature in riparian zone under low-temperature water infiltration.

Finally, this study considers both local and global sensitivity analysis methods to analyze the effect of each parameter on the model. The results by local sensitivity analysis method show that the model is most sensitive to hydraulic head (H), followed by Van Genuchten parameter α , permeability coefficient (K_s), water temperature (T), Van Genuchten parameter n , residual moisture content (θ_r), saturated moisture content (θ_s). The variation of each parameter is linear with the change of temperature field. The parameters which are positively related to the temperature field are T , α , θ_r and θ_s , which means the parameter value becomes larger, the temperature becomes larger, and vice versa. The parameters which are negatively related to the temperature field are H , K_s and n , and the results are consistent with the qualitative analysis. And through the global sensitivity analysis method, it can be seen that the impact of hydraulic head (H), water temperature (T), permeability coefficient (K_s) and Van Genuchten parameter α to the system is obvious, and the model is not sensitive to Van Genuchten parameter n , residual moisture content (θ_r), saturated moisture content (θ_s).

Acknowledgements

The authors thank Kenneth A. Kuhl, and a Literacy Volunteer of Leon County (Tallahassee, FL, United States) for his insightful comment that has helped to improve this manuscript. This study was funded by CRSRI Open Research Program (Grant No. CKWV2017500/KY), and National Natural Science Foundation of China (Grant No. 51679194), and State Key Laboratory of Eco-hydraulics in Northwest Arid Region of China (Xi'an University of Technology) (Grant No. 2016ZZKT-4).

References

- Anderson, M.P., 2005. Heat as a ground water tracer. *Ground Water* 43, 951–968.
- Bakker, M., Caljé, R., Schaars, F., van der Made, K.-J., de Haas, S., 2015. An active heat tracer experiment to determine groundwater velocities using fiber optic cables installed with direct push equipment. *Water Resour. Res.* 51, 2760–2772.
- Bowler, D.E., Mant, R., Orr, H., Hannah, D.M., Pullin, A.S., 2012. What are the effects of wooded riparian zones on stream temperature? *Environ. Evid.* 1, 3.
- Chung, S.O., Horton, R., 1987. Soil heat and water flow with partial surface mulch. *Water Resour. Res.* 23 (12), 2175–2786.
- Curtin, D., Beare, M.H., Hernandez-Ramirez, G., 2012. Temperature and moisture effects on microbial biomass and soil organic matter mineralization. *Soil Sci. Soc. Am. J.* 76 (6), 2055–2067.
- Contosta, A.R., Burakowski, E.A., Varner, R.K., Frey, S.D., 2016. Winter soil respiration in a humid temperate forest: the roles of moisture, temperature, and snowpack. *J. Geophys. Res.* 121 (12), 3072–3088.
- Constanz, J., 2008. Heat as a tracer to determine streambed water exchanges. *Water Resour. Res.* 44, W00D10. <http://dx.doi.org/10.1029/2008wr006996>.
- Colombani, N., Giambastiani, B.M.S., Mastrociccio, M., 2015. Combined use of heat and saline tracer to estimate aquifer properties in a forced gradient test. *J. Hydrol.* 525, 650–657.
- De Vries, 1963. Thermal properties of soils. In: Van Wijk, W.R. (Ed.), *Physics of Plant Environment*. John Wiley and Sons, Inc., New York, pp. 210–235.
- Doro, K.O., Cirpka, O.A., Leven, C., 2015. Tracer tomography: design concepts and field experiments using heat as a tracer. *Groundwater* 53, 139–148.
- Duque, C., Calvache, M.L., Engesgaard, P., 2010. Investigating river-aquifer relations using water temperature in an anthropized environment (Motril-Salobreña aquifer). *J. Hydrol.* 381, 121–133.
- Duque, C., Müller, S., Sebok, E., Haider, K., Engesgaard, P., 2016. Estimating groundwater discharge to surface waters using heat as a tracer in low flux environments: the role of thermal conductivity. *Hydrol. Process.* 30, 383–395.
- Gordon, R.P., Lutz, L.K., Briggs, M.A., McKenzie, J.M., 2012. Automated calculation of vertical pore-water flux from field temperature time series using the VFLUX method and computer program. *J. Hydrol.* 420–421, 142–158.
- Halloran, L.J.S., Rau, G.C., Andersen, M.S., 2016. Heat as a tracer to quantify processes and properties in the vadose zone: a review. *Earth Sci. Rev.* 159, 358–373.
- Hyun, Y.J., Kim, H.J., Lee, S.-S., Lee, K.-K., 2011. Characterizing streambed water fluxes using temperature and head data on multiple spatial scales in Munsan stream, South Korea. *J. Hydrol.* 402, 377–387.
- Hare, D.K., Briggs, M.A., Rosenberry, D.O., Boutt, D.F., Lane, J.W., 2015. A comparison of thermal infrared to fiber-optic distributed temperature sensing for evaluation of groundwater discharge to surface water. *J. Hydrol.* 530, 153–166.
- Irvine, D.J., Cranswick, R.H., Simmons, C.T., Shanfield, M.A., Lutz, L.K., 2015a. The effect of streambed heterogeneity on groundwater-surface water exchange fluxes inferred from temperature time series. *Water Resour. Res.* 51, 198–212.
- Irvine, D.J., Lutz, L.K., Briggs, M.A., Gordon, R.P., McKenzie, J.M., 2015b. Experimental evaluation of the applicability of phase, amplitude, and combined methods to determine water flux and thermal diffusivity from temperature time series using VFLUX 2. *J. Hydrol.* 531, 728–737.
- Kandelous, M., Šimunek, J., 2010. Numerical simulations of water movement in sub-surface drip irrigation system under field and laboratory conditions using HYDRUS-2D. *Agric. Water Manage.* 97 (7), 1070–1076.
- Keery, J., Binley, A., Crook, N., Smith, J.W.N., 2007. Temporal and spatial variability of groundwater-surface water fluxes: development and application of an analytical method using temperature time series. *J. Hydrol.* 336, 1–16.
- Klepikova, M.V., Borgne, T.L., Bour, O., Dentz, M., Hochreutener, R., Lavenant, M., 2016a. Heat as a tracer for understanding transport processes in fractured media: theory and field assessment from multiscale thermal push-pull tracer tests. *Water Resour. Res.* 52, 5442–5457.
- Klepikova, M., Wildemeersch, S., Hermans, T., Jamin, P., Orban, P., Nguyen, F., Brouyère, S., Dassargues, A., 2016b. Heat tracer test in an alluvial aquifer: field experiment and inverse modelling. *J. Hydrol.* 540, 812–823.
- Laganieri, L., Pare, D., Bergeron, Y., et al., 2012. The effect of boreal forest composition on soil respiration is mediated through variations in soil temperature and C quality. *Soil Biol. Biochem.* 53, 18–27.
- Maheu, A., St-Hilaire, A., Caissie, D., 2016. Understanding the thermal regime of rivers influenced by small and medium size dams in Eastern Canada. *River Res. Appl.* 32 (10), 2032–2044.
- Maurer, G.E., Bowling, D.R., 2014. Seasonal snowpack characteristics influence soil temperature and water content at multiple scales in interior western U.S. mountain ecosystems. *Water Resour. Res.* 50, 5216–5234.
- Mamer, E.A., Lowry, C.S., 2013. Locating and quantifying spatially distributed

- groundwater/surface water interactions using temperature signals with paired fiber-optic cables. *Water Resour. Res.* 49, 7670–7680.
- McCallum, A.M., Andersen, M.S., Rau, G.C., Acworth, R.I., 2012. A 1-D analytical method for estimating surface water-groundwater interactions and effective thermal diffusivity using temperature time series. *Water Resour. Res.* 48, W11532. <http://dx.doi.org/10.1029/2012WR012007>.
- Morris, M.D., 1991. Factorial sampling plans for preliminary computational experiments. *Technometrics* 33 (2), 161–174.
- Munz, M., Oswald, S.E., Schmidt, C., 2016. Analysis of riverbed temperatures to determine the geometry of subsurface water flow around in-stream geomorphological structures. *J. Hydrol.* 539, 74–87.
- Naranjo, R.C., Turcotte, R., 2015. A new temperature profiling probe for investigating groundwater-surface water interaction. *Water Resour. Res.* 51, 7790–7797.
- Preece, R.M., Jones, H.A., 2002. The effect of Keepit Dam on the temperature regime of the Namoi River, Australia. *River Res. Appl.* 18 (4), 397–414.
- Prats, J., Val, R., Armengol, J., Dolz, J., 2010. Temporal variability in the thermal regime of the lower Ebro River (Spain) and alteration due to anthropogenic factors. *J. Hydrol.* 387 (1–2), 105–118.
- Paul, K.I., Polglase, P.J., Smethurst, P.J., O'Connell, A.M., Carlyle, C.J., 2004. Soil temperature under forests: a simple model for predicting soil temperature under a range of forest types. *Agric. For. Meteorol.* 121 (3–4), 167–182.
- Riveros-Iregui, D.A., Emanuel, R.E., Muth, D.J., McGlynn, B.L., Epsterin, H.E., Welsch, D.L., Pacific, V.J., Wraith, J.M., 2007. Diurnal hysteresis between soil CO₂ and soil temperature is controlled by soil water content. *Geophys. Res. Lett.* 34 (17), L17404. <http://dx.doi.org/10.1029/2007GL030938>.
- Ren, J., Shen, Z.Z., Yang, J., Zhao, J., Ji-na Yin, J.N., 2014. Effects of temperature and dry density on hydraulic conductivity of silty clay under infiltration of low-temperature water. *Arab. J. Sci. Eng.* 39, 461–466.
- Sakata, Y., 2015. Heat as a tracer for examining depth-decaying permeability in gravel deposits. *Groundwater* 53, 21–32.
- Schneidewind, U., van Berkel, M., Anibas, C., Vandersteen, G., Schmidt, C., Joris, I., Seuntjens, P., Reeves, J., Hatch, C.E., 2016. Impacts of three-dimensional nonuniform flow on quantification of groundwater-surface water interactions using heat as a tracer. *Water Resour. Res.* 52, 6851–6866.
- Sellwood, S.M., Hart, D.J., Bahr, J.M., 2015. Evaluating the use of in-well heat tracer tests to measure borehole flow rates. *Ground Monit. Remediation* 35 (4), 85–94.
- Sawyer, A.H., Cardenas, M.B., Bomar, A., Mackey, M., 2009. Impact of dam operations on hyporheic exchange in the riparian zone of a regulated river. *Hydrol. Process.* 23, 2129–2137.
- Šimunek, J., van Genuchten, M.Th., Šejna, M., 2006. The HYDRUS software package for simulating two- and three-dimensional movement of water, heat, and multiple solutes in variably saturated media. Technical Manual. Version 1.0.
- Sophocleous, M., 1979. Analysis of water and heat flow in unsaturated-saturated porous media. *Water Resour. Res.* 15 (5), 1195–1206.
- Tonina, D., Luce, C., Gariglio, F., 2014. Quantifying streambed deposition and scour from stream and hyporheic water temperature time series. *Water Resour. Res.* 50, 287–292. <http://dx.doi.org/10.1029/2012WR012007>.
- van Genuchten, M. Th., 1980. A closed-form equation for predicting hydraulic conductivity of unsaturated soils. *Soil Sci. Soc. Am. J.* 44 (5), 892–898.
- Wang, R., Wang, Z.Q., Sun, Q.Q., Zhao, M., Du, L.L., Wu, D.F., Li, R.J., Gao, X., Guo, S.L., 2016. Effects of crop types and nitrogen fertilization on temperature sensitivity of soil respiration in the semi-arid Loess Plateau. *Soil Tillage Res.* 163, 1–9.
- Wilson, A., Woodward, G.L., Savidge, W.B., 2016. Using heat as a tracer to estimate the depth of rapid porewater advection below the sediment-water interface. *J. Hydrol.* 538, 743–753.
- Wildemeersch, S., Jamin, P., Orban, P., Hermans, T., Klepikova, M., Nguyen, F., Brouyère, S., Dassargues, A., 2014. Coupling heat and chemical tracer experiments for estimating heat transfer parameters in shallow alluvial aquifers. *J. Contam. Hydrol.* 169, 90–99.
- Xie, Y.Q., Cook, P.G., Simmons, G.T., Zheng, C.M., 2015. On the limits of heat as a tracer to estimate reach-scale river-aquifer exchange flux. *Water Resour. Res.* 51, 7401–7416.
- Yang, M.F., Li, L., Li, J., 2012. Prediction of water temperature in stratified reservoir and effects on downstream irrigation area: a case study of Xiahushan reservoir. *Phys. Chem. Earth, Parts A/B/C* 53–54, 38–42.